Article

Ag_3PO_4 enables the generation of long-lived radical cations for visible light-driven [2 + 2] and [4 + 2] pericyclic reactions

Lirong Guo[1], Rongchen Chu[1], Xinyu Hao[1], Yu Lei[2], Haibin Li[1], Dongge Ma [3], Guo Wang[4], Chen-Ho Tung[1] & Yifeng Wang [1] ✉

Photocatalytic redox reactions are important for synthesizing fine chemicals from olefins, but the limited lifetime of radical cation intermediates severely restricts semiconductor photocatalysis efficiency. Here, we report that Ag_3PO_4 can efficiently catalyze intramolecular and intermolecular [2 + 2] and Diels-Alder cycloadditions under visible-light irradiation. The approach is additive-free, catalyst-recyclable. Mechanistic studies indicate that visible-light irradiation on Ag_3PO_4 generates holes with high oxidation power, which oxidize aromatic alkene adsorbates into radical cations. In photoreduced Ag_3PO_4, the conduction band electron (e_{CB}^-) has low reduction power due to the delocalization among the Ag^+-lattices, while the particle surfaces have a strong electrostatic interaction with the radical cations, which considerably stabilize the radical cations against recombination with e_{CB}^-. The radical cation on the particle's surfaces has a lifetime of more than 2 ms, 75 times longer than homogeneous systems. Our findings highlight the effectiveness of inorganic semiconductors for challenging radical cation-mediated synthesis driven by sunlight.

Aromatic alkene radical cations, which are one electron (1e)-oxidation intermediates of aromatic alkenes, play important roles in the synthesis of complex functionalized molecules and cyclic moieties, particularly the [2 + 2] and [4 + 2] pericyclic products. To generate and make use of aromatic alkene radical cations, extensive efforts have been devoted for a long time. Compared to single electron oxidants such as Ce^{4+1}, Fe^{3+2}, and hypervalent iodine reagents[3,4], photocatalysts (PCs) generate highly oxidizing holes under sunlight irradiation and operate under mild conditions, making photocatalysis a green and sustainable strategy for radical cation-mediated reactions[5–16]. However, the PCs utilized for generating radical cations are primarily homogeneous organic compounds, particularly transition metal-coordination complexes[8–11] and π-conjugated molecules[12–15]. Meanwhile, the scope of the approaches is constrained by the short lifetime

of radical cations (on a μs scale[17–23]). In contrast, inorganic semiconductor PCs (isPCs), such as TiO_2, CdS, Bi_2MoO_6, and Ag_3PO_4, have been widely employed for solar light harvesting applications, including water splitting, organic pollutant degradation, and photoelectric conversion[24]. From a practical standpoint, they are generally considered stable, recyclable, inexpensive, and environmentally friendly, making them an ideal choice for use in photosynthesis[25]. However, the efficiency of isPCs in the 1e-oxidative activation of non-polar and non-coordinative C = C moieties on their surfaces is typically low[17,20,26–33]. One obstacle is the short lifetime of holes (fs to ns[34]), which significantly slows down the 1e-oxidation of the C = C moieties (Fig. 1a). Moreover, even if some alkene radical cations are slowly generated at the surfaces of a traditional isPC like TiO_2, they undergo few intermolecular C-C formation reactions[17]. Instead, they are more prone to

[1]Key Lab for Colloid and Interface Science of Ministry of Education, School of Chemistry and Chemical Engineering Shandong University Jinan, 250100 Jinan, China. [2]Key Laboratory of Photochemistry, Institute of Chemistry Chinese Academy of Sciences Beijing, 100190 Beijing, China. [3]College of Chemistry and Materials Engineering Beijing Technology and Business University Beijing, 100048 Beijing, China. [4]Department of Chemistry Capital Normal University Beijing, 100048 Beijing, China. ✉e-mail: yifeng@sdu.edu.cn
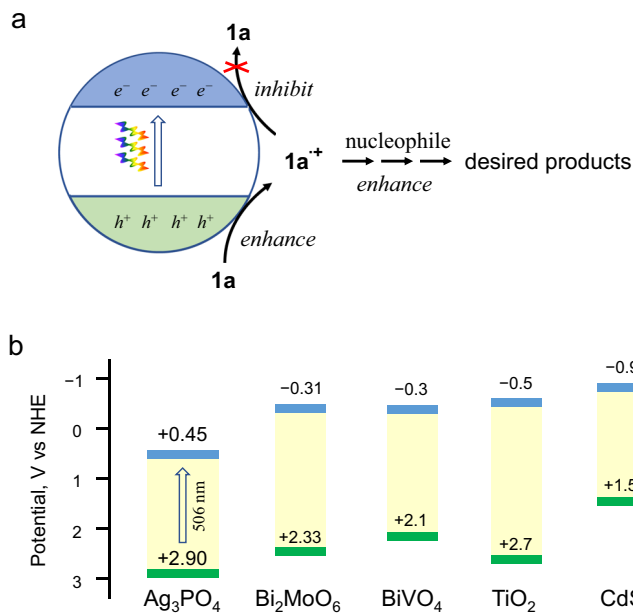
a

b

Fig. 1 | The selection of an inorganic semiconductor for photocatalytic pericyclic reactions. a Requirements for using anethole radical cation (**1a**⁺) in photocatalytic constructing functionalized molecules from anethole (**1a**). **b** The band positions of Ag₃PO₄ and commonly applied photocatalysts.

Fig. 2 | The model reaction of 1a. Conditions: **1a**, 1 mmol; Ag₃PO₄, (27 mg, 0.12 equiv); HFIP, 3.0 mL; LED (425 nm); 1 atm N₂; 0 °C; 12 h.

nucleophilic attack by long-lived photogenerated electrons (e_{CB}^-), resulting in ineffective 1e-oxidation. These hindrances lead to a diminished quantum yield of light (i.e. reduced reaction rate) and low product yield, regardless of reaction time. Therefore, it is imperative to extend the lifespan of alkene radical cations for affordable and recyclable PCs that can effectively harvest sunlight for pericyclic reactions. However, this remains an ongoing challenge.

Among all the available isPCs, Ag₃PO₄ stands out as one of the few that exhibits an inherent visible-light response[35]. It has been extensively used in visible-light-driven water oxidation[35–37] and organic pollutant degradation[37,38]. Compared to other commonly used semiconductors, it produces strong oxidizing holes and weak reducing electrons under visible-light irradiation (+2.9 V and +0.45 V *vs.* NHE; Fig. 1b). Moreover, the surfaces of Ag₃PO₄ are rich in large PO₄³⁻ anions with high charge density that can strongly electrostatically interact with cationic species such as radical cations. As a result, photo-excited Ag₃PO₄ may efficiently generate but inefficiently quench radical cations, allowing for the accumulation of radical cations to facilitate radical cation-mediated reactions.

In this work, we demonstrate that Ag₃PO₄ efficiently catalyzes intramolecular and intermolecular [2 + 2] and Diels-Alder cycloadditions under visible light or solar irradiation. The system exhibits remarkable efficiency with respect to substrate scope, product yield, diastereoselectivity, apparent quantum yield (AQY), and scaleup synthesis under solar irradiation. Two critical aspects of the reaction mechanism are validated: (1) the existence of long-lived **1a**⁺ radical cations on the surfaces of Ag₃PO₄ that are photo-reduced in situ, (2) the acceleration of rate-limiting step by prolonging the lifetime of **1a**⁺. Our discoveries may pave the way for employing highly active organic radical cations and even radical anions in critical pericyclic processes.

Results

Transformation of aromatic alkene 1a to *anti*-cyclobutane 2a

Anethole (**1a**) has been the most studied electron-rich β-substituted styrene in [2 + 2] cycloaddition reactions[3,19,39]. Therefore, it was selected as the model compound to evaluate the photocatalytic performance of Ag₃PO₄ (Fig. 2). A self-synthesized Ag₃PO₄ sample composed
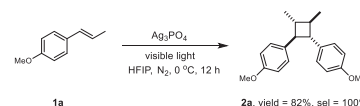
of nanospheres with a diameter of 230 ± 60 nm was used for the study (Fig. 3a). The cycloaddition reaction was conducted under an N₂ atmosphere by irradiating a suspension of reactant **1a** in hexafluoroisopropanol (HFIP) solvent containing a catalytic quantity of Ag₃PO₄ (9.0 g L⁻¹ dosage, 0.12 equiv) at 0 °C. No additive was introduced. The conversion of **1a** proceeded smoothly, affording *anti*-cyclobutane **2a** as the sole product (see Supplementary Fig. 1 for the time-resolved ¹H NMR spectra and kinetics). After 12 h of reaction, the yield of **2a** reached 82%, with a high diastereoselectivity (*d.r.* > 19:1). Further irradiation did not affect conversion due to equilibration between **1a** and **2a** (Supplementary Fig. 2), as commonly observed in photocatalyzed radical cation processes[39,40]. Due to this equilibrium, the 82% yield was also achieved using various Ag₃PO₄ samples, including a commercially available Ag₃PO₄ and several self-synthesized faceted Ag₃PO₄ nanocrystal samples (see Supplementary Table 1 for screening of the experimental conditions). This implies that the catalyst is easily accessible.

The control experiments demonstrated that in the absence of Ag₃PO₄ or light, no conversion of **1a** occurred (Supplementary Table 1). Therefore, both light and Ag₃PO₄ are indispensable for the reaction, excluding the possibility of a thermocatalytic mechanism. Notably, the [2 + 2] cycloaddition reaction requires an inert atmosphere. Under air atmosphere, the conversion of **1a** could reach 100%, but 4-methoxybenzaldehyde was the main product (82% yield). The yield of the cycloaddition product **2a** was only 13%. This suggests that Ag₃PO₄ facilitates the selective oxidation of aromatic alkenes, resulting in the formation of the corresponding aromatic aldehydes, when O₂ participates in the reaction process. We also performed the reaction in other solvents like tetrahydrofuran (THF), MeOH, EtOAc, and CF₃CH₂OH, but they were not as effective as HFIP. As shown in Fig. 3b, Ag₃PO₄ can effectively harvest visible light up to 500 nm to initiate the **1a** → **2a** cycloaddition, which is close to its absorption edge. The AQY values were determined according to the initial 30-min yields. The action spectrum of AQY matches the UV-vis diffuse-reflectance spectrum of Ag₃PO₄. The UV-vis absorption spectrum of **1a** shows it can only absorb light below 320 nm, and only Ag₃PO₄ can be excited by the light source (Supplementary Fig. 3). Although we were aware that depositing AgNPs on the surfaces of Ag₃PO₄ could enhance its photoabsorption and charge-separation efficiency[41], our experiments using AgNPs-loaded samples with different AgNPs' loadings afforded lower yields than pure Ag₃PO₄. Furthermore, as the loading of AgNPs increased, the final yield of **2a** decreased (Supplementary Figs. 4−6). This suggests that AgNPs are not the photocatalyst and can inhibit the activity of Ag₃PO₄. In all, it can be concluded that Ag₃PO₄ is the true photocatalyst, and all **2a** is the product of Ag₃PO₄ photocatalysis.

Silver salt-based photocatalysts often suffer from photocorrosion[42–45]. However, in the current system, the 0.12 equiv of initially added Ag₃PO₄ successfully worked five consecutive photocatalytic cycles with only a slight decrease in efficiency (Fig. 3c), resulting in a turnover number of 13. Photo-corrosion of Ag₃PO₄ was observed, as evidenced by its significant darkening after five cycles. The TEM image indicates the formation of numerous AgNPs on the surfaces of Ag₃PO₄ (Supplementary Fig. 7). Nevertheless, regeneration of the recycled sample was achieved through a simple immersion in 6.7 mM Na₂HPO₄ aqueous solution and the addition of a drop of 30% H₂O₂[46]. Within minutes, color, microscopic morphology, and photocatalytic performance were fully restored (Supplementary Fig. 7). As
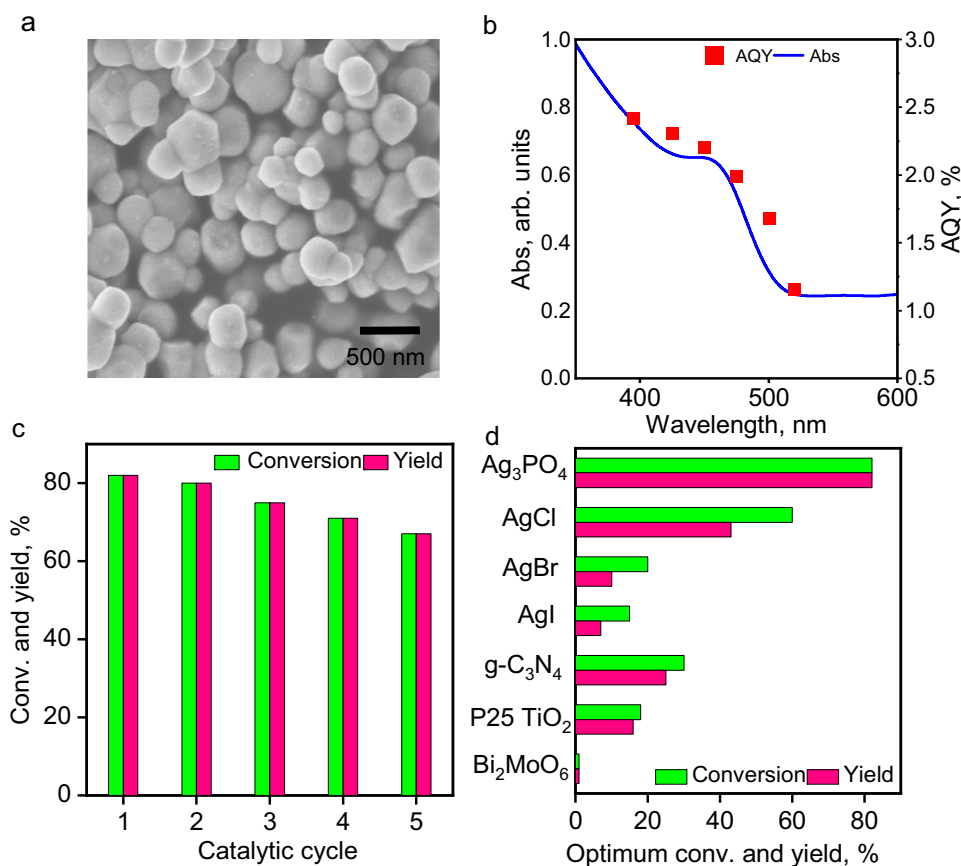
Fig. 3 | Characterization of Ag$_3$PO$_4$ and the yields of 2a under various conditions. a An SEM image of Ag$_3$PO$_4$. **b** The UV-vis diffuse-reflectance spectrum (smooth blue curve) and the AQY action spectrum (red diamond marks; see Supplementary Information for calculation method) of Ag$_3$PO$_4$. **c** The conversion of **1a** (green) and yield of **2a** (red) during reuse of Ag$_3$PO$_4$. **d** The conversion of **1a** (green) and yield of **2a** (red) by various photocatalysts. The unspecified conditions in panels **b**–**d**: **1a**, 0.5 mmol; catalyst, 0.12 equiv; HFIP, 1.5 mL; light source, 425 ± 10 nm LED (120 mW cm^{-2}); N$_2$ atmosphere; 0 °C; 12 h. In panel **d**, a 395 ± 10 nm LED lamp (119 mW cm^{-2}) was used for TiO$_2$. The reaction time was optimized for each photocatalyst, reaching up to 24 h for TiO$_2$. The yields were determined by ^{1}H NMR using 4-ethoxybenzaldehyde as the internal standard.

shown in Fig. 3d, when the other silver salts, such as AgCl, AgBr, and AgI, were used, the conversion of **1a** and the selectivity of **2a** were significantly lower than that of Ag$_3$PO$_4$. Both commercially available and self-synthesized AgCl, AgBr, and AgI decomposed rapidly upon irradiation (see Supplementary Fig. 8 for characterization). In comparison to the widely studied heterogeneous photocatalysts[47], including graphitic carbon nitride (g-C$_3$N$_4$), Bi$_2$MoO$_6$, and TiO$_2$, the performance of Ag$_3$PO$_4$ is superior. For example, the reaction rate was notably low over TiO$_2$ even under UV. Furthermore, electron accumulation caused TiO$_2$ to exhibit a blue hue and ultimately became completely inert once conversion reached 18% (Supplementary Fig. 9). When TiO$_2$ was used under air atmosphere, the accumulated electrons can be efficiently quenched by O$_2$. However, in this case the yield of **2a** was less than 10% due to the over-oxidization of **1a** to 4-methoxybenzaldehyde (67%). Supplementary Table 2 shows that Ag$_3$PO$_4$ performs comparably to state-of-the-art PCs and single-electron oxidants such as Ru(bpm)$_3$(BArF)$_2$[39], PhI(OAc)$_2$[3] and Fe(ClO$_4$)$_3$[19] in the **1a** → **2a** cycloaddition[19]. Therefore, Ag$_3$PO$_4$ is highly applicable for [2 + 2] cyclobutanation reactions.

Ag$_3$PO$_4$/visible light system for pericyclic reactions

Given the success of the [2 + 2] homo-cycloaddition of **1a**, we sought to explore whether the Ag$_3$PO$_4$/visible light system could serve as a versatile tool for achieving various pericyclic reactions. Our initial focus was on investigating the scope of the intermolecular dimerization reaction. As shown in Fig. 4, a diverse range of electron-rich aromatic alkenes with varying substituents underwent smooth reaction, affording the corresponding symmetrical cyclobutanes in moderate to good yields and excellent diastereoselectivity (**2a**-**2h**, yield ranges 42%-83%, *d.r.* > 19:1). Electronic density of the aromatic ring and steric hindrance at the β-site exert a noticeable influence on the reaction outcome (**2b** vs. **2c**, **2a** *vs.* **2d**-**2f**). However, this catalytic system exhibits high tolerance toward steric hindrance at the benzene ring (**2a** *vs.* **2f**-**2h**). Notably, NO$_2$-, OH-, and COOH-substituted aromatic alkenes were challenging substrates for other [2 + 2] cycloaddition catalytic systems[48], as well as the current Ag$_3$PO$_4$ system (Supplementary Table 3). Finally, we achieved a 70% isolated yield of magnosalin (**2h**), a valuable natural product. We then used the system to synthesize unsymmetric cyclobutanes and were pleased to discover that a variety of aromatic alkenes, including unsubstituted aromatic alkene (**4a**) and substituted aromatic alkenes with electron-donating groups (EDGs; **4b**, **4d**, **4i**) and electron-withdrawing groups (EWGs; **4c**, **4e**, **4f**, **4g**, **4h**) at both ortho-, meta- and para-sites of the benzene rings, could be employed as model reaction counterparts using **1a**. The corresponding intermolecular [2 + 2] products (**2a**–**2h** and **4a**–**4i**) were obtained in high yields and high regioselectivity (head-to-head; see Supplementary Table 4 for ^{1}H NMR analysis). The sole byproduct resulting from these crossed reactions is the homo-cycloaddition product, e.g., **2a**. However, because the crossed reactions are much faster than the homo-cycloaddition (see Supplementary Fig. 10 for a comparison of the rates), introducing **1a** via a syringe pump would inhibit the homo [2 + 2] reaction. Next, we explored the feasibility of intramolecular
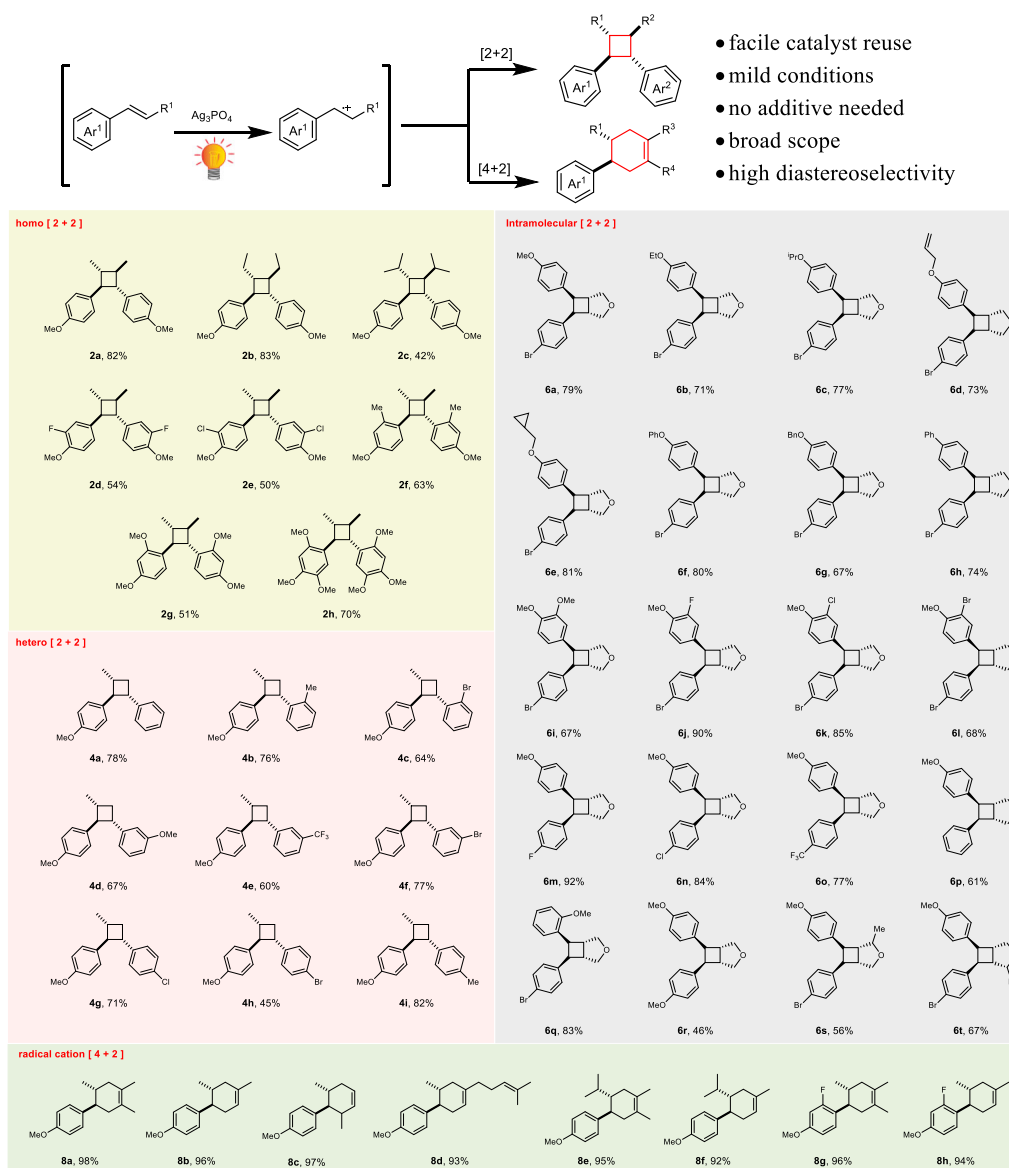
Fig. 4 | Scope of the Ag$_3$PO$_4$ photocatalysis in the radical cation pericyclic reactions. [a]Conditions for homo [2 + 2] reactions: substrate, 1.0 mmol; Ag$_3$PO$_4$, 27 mg (0.12 equiv); 12–18 h. [b]Conditions for hetero [2 + 2] reactions: **1a**, 0.5 mmol; the counterpart, 1.0 mmol; Ag$_3$PO$_4$, 44 mg (0.20 equiv); 12 h. [c]Conditions for intramolecular [2 + 2] reactions: substrate, 0.3 mmol; Ag$_3$PO$_4$, 12 mg (0.10 equiv); 12 h. [d]Conditions for [4 + 2] reactions: aromatic alkene, 1.0 mmol; diene, 2.0 mmol; Ag$_3$PO$_4$, 32 mg (0.08 equiv); 8 h.

[2 + 2] cycloaddition, an efficient approach for synthesizing fused heterocycles[6]. Strikingly, all tested bis(styrene)s afforded good to excellent yields of the desired cyclobutanes (**6a-6t**). The intramolecular [2 + 2] cycloadditions exhibit a broad tolerance toward EDGs, EWGs, and the steric hindrance at both the benzene ring and the β-site. The Diels-Alder reaction is considered one of the essential C-C bond-forming reactions in synthetic organic chemistry. Recent studies have shown that photocatalytic methods are effective in the radical-cation-mediated cycloadditions of electron-rich olefins and dienes[32,49–52], which are challenging substrates for conventional thermal processes. In this study, we found that even with a reduced Ag$_3$PO$_4$ loading of 0.08 equiv, the Ag$_3$PO$_4$/visible light system was still capable of facilitating Diels-Alder cycloadditions involving the radical cations. Moreover, the 0.08 equiv of Ag$_3$PO$_4$ was successfully reused for five consecutive runs without any noticeable decrease in performance (Supplementary Figure 11). Based on the substituted aromatic alkenes, the yields achieved in all tested reactions are near unity (**8a-8h**). The products **8b, 8c, 8d, 8f, and 8h** were isolated in high regioselectivity

without isomers. This can be attributed to the large steric hindrance of the butadiene side chain (see Supplementary Table 4 for ^{1}H NMR analysis).

The remarkable diastereoselectivity of the reactions is noteworthy. Specifically, nearly all intermolecular [2 + 2] products are anti; intramolecular [2 + 2] products are predominately syn, and nearly all Diels-Alder reactions yield anti-products.

Scale synthesis of [2 + 2] and [4 + 2] reactions

To investigate the synthetic potential of the Ag$_3$PO$_4$/visible light system, we performed large-scale [2 + 2] and [4 + 2] reactions under natural sunlight irradiation by placing the reaction flasks on a windowsill at outdoor temperatures (1–10 °C). The sunlight intensity ranged from 15−23 mW cm^{-2}. Interestingly, 41.5 g of the [4 + 2] cycloaddition product **8a** was obtained almost quantitatively in a one-pot reaction after only six hours of irradiation (Fig. 5). After being filtered through diatomite, the Ag$_3$PO$_4$ solid was removed, resulting in nearly pure **8a** (41.5 g), which confirms the method's flexibility and ease of use. The
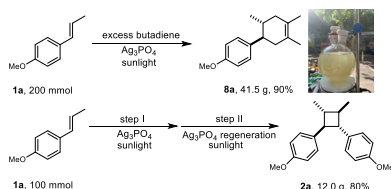
Fig. 5 | Scaleup synthesis using sunlight. Detailed reaction conditions were described in the Supplementary Information.

intermolecular [2 + 2] homo-cycloaddition of **1a** yielded a 60% yield of **2a** (100% selectivity) before Ag_3PO_4 (0.05 equiv) became deactivated. However, upon reintroduction of regenerated Ag_3PO_4 into the catalytic system, a final yield of 80% of **2a** was achieved (Fig. 5). The use of a 425 nm LED lamp achieved yields of **8a** that are comparable to that achieved by sunlight (Supplementary Table 1). Hence, the Ag_3PO_4/visible light system could facilitate actual industrial production considering the advances in LED technology.

Supplementary Tables 5–7 demonstrate the superior performance of the Ag_3PO_4/visible light system compared to the state-of-art reports in [2 + 2] and Diels-Alder cycloadditions. The current system boasts one of the highest efficiencies in heterogeneous systems, with broad light absorption. It is capable of realizing intramolecular and intermolecular [2 + 2] cycloadditions and Diels-Alder reactions.

Mechanism study and DFT simulations

Laser flash photolysis (LFP) was performed to detect the transient species involved in the photocatalytic **1a** → **2a** cycloaddition. The LFP transient absorption spectra of the **1a**/Ag_3PO_4/HFIP suspension were obtained in transmission mode. The representative spectra are depicted in Fig. 6a. The two distinct, intense peaks centered at ca. 387 and 605 nm precisely match the spectra of **1a**[+] generated by photolysis of homogeneous solutions of **1a**/H_2O-MeCN at 266 nm[53] and **1a**/MeCN at 308 nm[54], respectively, as reported in previous studies. Figure 6b demonstrates that the absence of **1a** or Ag_3PO_4 resulted in no signal from a 355-nm laser pulse, indicating the indispensability of both **1a** and Ag_3PO_4 for the formation of **1a**[+]. Hence, the LFP spectra confirm that photogenerated h^+ of Ag_3PO_4 facilitates the 1e-oxidation of **1a** to afford **1a**[+].

The concentration of a transient species, which is determined by both formation rate and lifetime, is essential for detecting it via LFP. Hence, the observation of **1a**[+] in the **1a**/Ag_3PO_4/HFIP system suggests that **1a**[+] forms rapidly and has a long life, allowing for its accumulation due to its formation far exceeding decay. Recall Fig. 6a, the sample initially exhibited strong background absorption, which significantly decreased after 250 μs due to the sedimentation of Ag_3PO_4 particles. The spectra at 250 and 500 μs showed similar level of background absorption, indicating that sedimentation was minor during this period. Based on this understanding, we measured the decay kinetics of **1a**[+] in the **1a**/Ag_3PO_4/HFIP suspension at $\lambda = 600$ nm. Figure 6c demonstrates that the signal intensity decayed significantly before 500 μs, which could be mostly attributable to the sedimentation mentioned above of Ag_3PO_4. Afterward, the signal intensity remained nearly constant until 1900 μs. This must not be attributed to the continuous generation of **1a**[+] by the photogenerated holes of Ag_3PO_4 after LFP, because it is well-known that the photogenerated holes in semiconductors are transient species. Instead, this indicates that the lifetime of **1a**[+] in the **1a**/Ag_3PO_4/HFIP system is more than 1900 μs.

We conducted light-on-off experiments to investigate the lifetime of **1a**[+] in the **1a**/Ag_3PO_4/HFIP system. The reaction vial was either left stirring in the dark after turning off the light or centrifuged to settle down the Ag_3PO_4 before being left in the dark. In the former situation, over the next six hours, there was a gradual increase of ca. 8% in yield of **2a** (Fig. 6d). This is distinct from the homogeneous systems, where the

1a → **2a** cycloaddition practically ceased upon light-off[55]. In the dark reaction without agitation, the yield of **2a** remained unchanged after Ag_3PO_4 settled down (Fig. 6d). It indicates that the long-lived **1a**[+] radical cations must remain adsorbed on the surfaces of the reduced Ag_3PO_4 (denoted as $(Ag_3PO_4)^{n-}$, where n is the number of e_{CB}^- per NP). When all the Ag_3PO_4 particles settled down, the **1a** molecules in solution could not reach **1a**[+], and thus the cycloaddition ceased. This verifies that the signals originate from **1a**[+] adsorbed on the Ag_3PO_4 surfaces rather than in the solution bulk. Further, it confirms that the radical cation-mediated [2 + 2] pericyclic reaction occurs on the surfaces of Ag_3PO_4 rather than in the solution.

It was reported that the decay rate constant[53,56] of **1a**[+] is $4 \times 10^4 \, s^{-1}$ in aerated MeCN, corresponding to a very short lifetime of 25 μs[54]. This is likely why the **1a** → **2a** cycloaddition stopped nearly instantly upon light-off in homogeneous systems[22,55]. To probe the lifetime of **1a**[+] in neat HFIP, we used a 266-nm laser pulse to excite a **1a**/HFIP solution. However, the system produced signals from unknown species and the absorption peaks of **1a**[+] at ca. 387 and 605 nm were not detected. This may suggest that the lifetime of **1a**[+] in HFIP is too short, resulting in a **1a**[+] concentration below the detection limit. We also used a 355-nm laser pulse to excite the **1a**/TiO_2/HFIP system, which produced a 16% yield of **2a**, indicating that photo-excited TiO_2 NPs generated **1a**[+]. However, the transient spectrum of **1a**[+] was not detected by LFP (Supplementary Fig. 12), implying that its lifetime in the system is also very short.

We found that the adsorption of reactant **1a** and desorption of product **2a** are crucial in the reaction. Figure 7a shows that the adsorption of **1a** on the (100)-facet-rich spherical Ag_3PO_4 (as the representative example) can fit well to the Langmuir type-I isotherm (Eq. 1),

$$\Gamma = \Gamma_m \cdot K \cdot C_{eq} / (1 + K \cdot C_{eq}) \tag{1}$$

where Γ is the adsorbed amount at the adsorption/desorption equilibrium concentration C_{eq}. The Langmuir coefficient K and the capacity of adsorption Γ_m are calculated to be $5.8 \pm 0.6 \, M^{-1}$ and $2.9 \pm 0.1 \, mmol \, g^{-1}$, respectively. In contrast, the adsorption of **2a** on Ag_3PO_4 surfaces is barely detectable, indicating very weak adsorption of **2a**.

At low **1a** concentrations, the AQY values increase dramatically with the initially added concentration of **1a** but then approach a plateau (Supplementary Fig. 13). This differs from a typical homogeneous bimolecular reaction, which is second order depending on the substrate concentration. Instead, the AQY values are well linearly correlated with the square of the fractional coverage of **1a**, Θ (Eq. 2),

$$AQY = k(\Gamma / \Gamma_m)^2 = k \, \theta^2 \tag{2}$$

where k denotes the slope of the plot (Fig. 7b). This kinetic equation corroborates that the conversion of **1a** through photocatalysis occurs on the Ag_3PO_4 surface. The rate-limiting step (RLS) of the formation of **2a** involves two molecular species of **1a** adsorbed on the surface. We also observe a significant solvent effect in the performance of Ag_3PO_4 in the **1a** → **2a** cycloaddition reaction (Fig. 7c). Ag_3PO_4 did not perform well in EtOAc, n-hexane or CH_2Cl_2, but performed better in CH_3CN, MeNO_2, and TFE, and performed best in HFIP. Surprisingly, Eq. 2 applies to the results from different solvents. Thus, solvents influence the AQY by modulating the **1a** distribution between the bulk solution and Ag_3PO_4 surfaces. It has been reported that the facets of photocatalysts substantially influence their activities, especially in the case of Ag_3PO_4[36,37,57,58]. For the **1a** → **2a** cycloaddition reaction, we used the spherical, rhombic dodecahedral, cubic, and tetrahedral NPs of Ag_3PO_4, which are rich in {100}, {110}, {100}, and {111} facets, respectively[36]. Figure 7d displays distinct AQYs on different facets and Eq. 2 is applicable to the results from various Ag_3PO_4 facets. Overall, Fig. 7 indicates that the photocatalytic cycloaddition reaction on
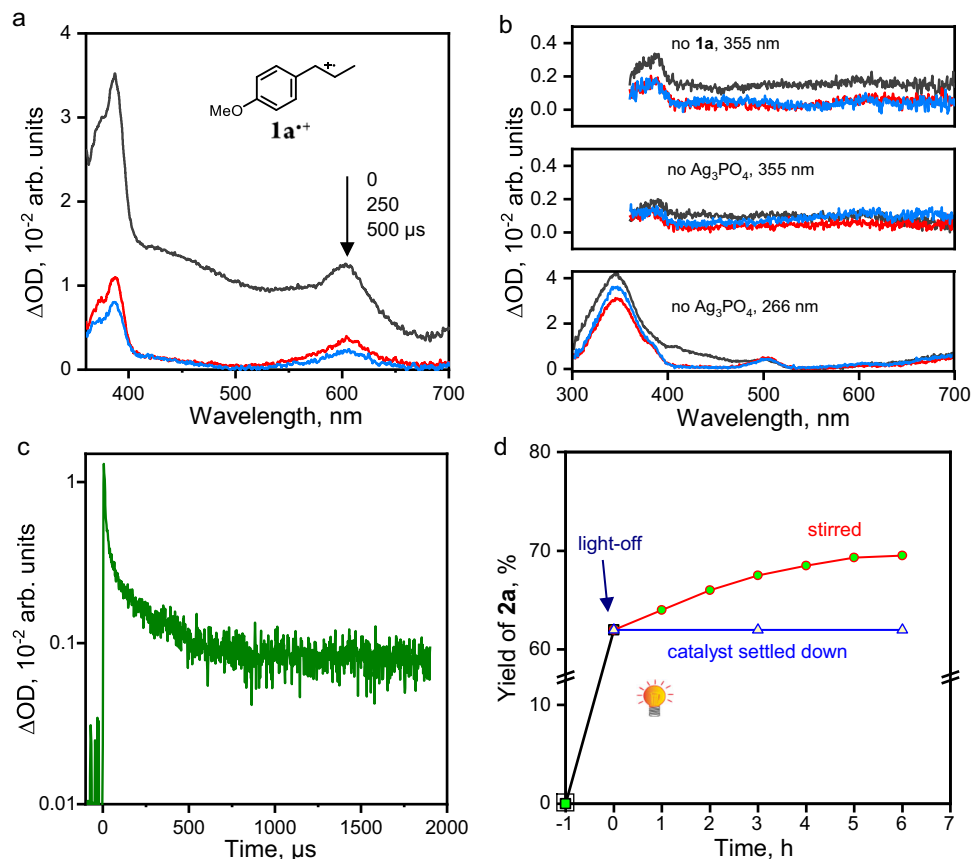
Fig. 6 | Detection of the transient species. a Transient absorption spectra of **1a**$^{•+}$ obtained at various times after a 10-ns 355-nm pulse irradiation of the **1a**/Ag$_3$PO$_4$/HFIP system at room temperature under an air atmosphere. Before LFP, the suspension was ultrasonicated for 30 min to enhance the dispersion of Ag$_3$PO$_4$ in HFIP.

b The transient absorption spectra obtained without **1a** or Ag$_3$PO$_4$: black, $t = 0$; red, 250 μs; blue, 500 μs. **c** The decay kinetics of **1a**$^{•+}$ after 355-nm pulse irradiation. **d** The kinetics of **2a** formation in the light on-off experiment.

Ag$_3$PO$_4$ surfaces follows the Langmuir-Hinshelwood mechanism for a bimolecular reaction. It also implies that the interaction between **1a** and Ag$_3$PO$_4$ surfaces is vital in the success of Ag$_3$PO$_4$ in the photocatalytic [2 + 2] cycloadditions.

We conducted DFT simulations to determine the mechanism of interfacial interactions between **1a** (and **2a**) and the Ag$_3$PO$_4$ surfaces. Given the substantial dimensions of the Ag$_3$PO$_4$ particles and the comparable sizes of **1a** or **2a** molecules to only a few phosphate anions, it is reasonable to regard the surface of Ag$_3$PO$_4$ particles as an infinitely expansive plane for adsorbing **1a** and **2a**. As the (100) facet is the lowest-energy facet of Ag$_3$PO$_4$ crystals[36,37,58] and the primary surface of spherical Ag$_3$PO$_4$, we selected the PO$_4$$^{3-}$-terminated and the Ag$^+$-terminated (100) facets to calculate the optimal adsorption configurations (see Supplementary Figs. 14–15 for details of results). Figure 8 displays the lowest-energy configurations of **1a** and **2a** molecules on the PO$_4$$^{3-}$-terminated (100) facet. It should be noted that the size of PO$_4$$^{3-}$ is much larger than that of Ag$^+$ (2.38 Å vs. 0.67 Å), but comparable to molecule **1a** in size. Molecule **1a** lies parallel to the facet, with its long axis aligned with the *a*-axis of the crystal lattice, and the CH = CH moiety positioned close to the O^{2-} ions of PO$_4$$^{3-}$. In this configuration, each **1a** molecule intimately contacts four PO$_4$$^{3-}$ anions, maximizing the interfacial interaction between **1a** and the Ag$_3$PO$_4$ surface. The strong interaction is consistent with the previously discussed adsorption of **1a** to the Ag$_3$PO$_4$ surfaces. This adsorption mode should be beneficial for the 1e-oxidation of the CH = CH moiety upon photo-excitation of Ag$_3$PO$_4$ since photogenerated holes are localized at O of PO$_4$$^{3−59}$. The energy required for adsorption of each **1a** molecule from the vacuum is −2.10 eV (Fig. 8a, b). In contrast, the calculated energies for **1a**

adsorption onto PO$_4$$^{3-}$-terminated (100) facet along the *b*-axis and that onto the Ag$^+$-terminated (100) facet along both the *a*- and *b*-axis, are substantially smaller at −1.67, −1.54, and −1.54 eV, respectively (Supplementary Fig. 14). These lower adsorption energies can be attributed to the greater spacing between the adjacent PO$_4$$^{3-}$ anions on these facets, which weakens the contact between **1a** and PO$_4$$^{3-}$. However, due to the large steric effects of the **2a** molecule, each **2a** has an optimum adsorption energy of −1.56 eV when adsorbed on the PO$_4$$^{3-}$-terminated (100) facet (Fig. 8c, d). The above calculations reveal a large adsorption energy difference between two **1a** and one **2a**, i.e. +2.64 eV on the PO$_4$$^{3-}$-terminated Ag$_3PO_4$ (100) facet in a vacuum. The much weaker adsorption of **2a** suggests that the **1a**→**2a** cycloaddition on the Ag$_3$PO$_4$ surfaces benefits from the easier removal of product **2a**.

The atomic Bader charges shown in Fig. 8e indicate that the electron density of **1a** changes upon adsorption. The overall Bader charge of adsorbed **1a** is 0.34e, indicating a transfer of 0.34e from **1a** to the Ag$_3$PO$_4$ surfaces during adsorption. The two H-atoms in the CH = CH moiety have enormous Bader charges, namely, 0.1323e and 0.1e, respectively. This, combined with the very negative Bader charge of the CH$_3$O moiety (−0.4587e), strongly suggests that polarization occurs in molecule **1a** and that its CH = CH group is activated upon adsorption. The high Bader charge also means that the CH = CH group is the most readily oxidized site in **1a**.

Figure 9 illustrates a plausible mechanism for Ag$_3$PO$_4$ triggering the [2 + 2] cycloaddition of **1a** under visible-light irradiation. Initially, Ag$_3$PO$_4$ adsorbs **1a** molecules on its surface via PO$_4$$^{3-}$ anions (step I). Then, upon excitation, Ag$_3$PO$_4$ generates many e_{CB}^- in the conduction band and h^+ in the valance band (step II). Due to the fact that the
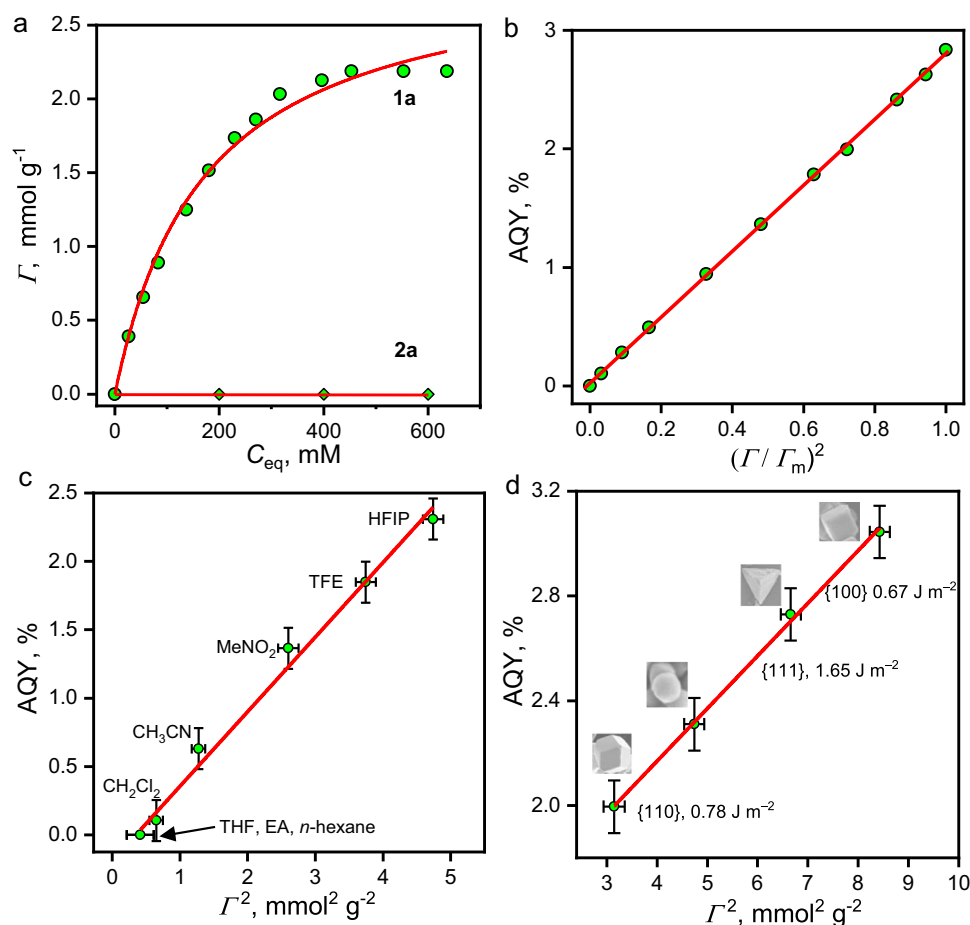
Fig. 7 | Dependence of AQY on adsorption. a The adsorption isotherm of **1a** and **2a** on spherical Ag_3PO_4. **b–d** The AQY values of the **1a** → **2a** cycloaddition reaction as functions of $(\Gamma/\Gamma_m)^2$ or Γ^2. The scattered points represent the experimental values, and the red lines are the curve fit or linear fits. Abbreviations for panel **c**: THF tetrahydrofuran, EA ethyl acetate, TFE trifluoroethanol. The SEM images, facets, and surface energies of Ag_3PO_4 NPs are indicated in panel d. The error bars in panels (**c**) and(**d**) associated with AQY represent the standard error of three sets of unique measurements.

conduction band bottom is mainly composed of hybridized Ag 5s5p orbitals[35], the reduction power of the electrons in the conduction band of Ag_3PO_4 is low (E_{CB} = +0.45 V vs. NHE[35,41,60,61]). The unreactive e_{CB}^- remains in the form of $(Ag^{\delta+})_m^-$, which means it is shared by many Ag^+ ions. The observed AgNP formation substantiates that e_{CB}^- transfers to Ag^+ ions. The valance band top of Ag_3PO_4 mainly comprises hybridized O 2p and Ag 4d orbitals. The h^+ in the valence band has strong oxidation power (E_{VB} = +2.90 V vs. NHE[35,41,60,61]) and is able to gain an electron from the CH = CH group of **1a** to yield **1a**$^{•+}$ (step III). The 1e-oxidation of **1a** results in the photocatalytically reduced NP with numerous e_{CB}^-. The **1a**$^{•+}$ species strongly adsorbs on the surfaces of $(Ag_3PO_4)^{n-}$. In this case, the electrostatic interaction between **1a**$^{•+}$ and $(Ag_3PO_4)^{n-}$ NP surfaces is analogous to the interactions in homogeneous solutions described by Yoon et al. for **1a**$^{•+}$ with a tetraarylborate anion[18], Ishihara et al. for **1a**$^{•+}$ with $FeCl_4^-$[19–21], and List et al. for **1a**$^{•+}$ with an imidodiphosphorimidate counteranion[22].

The adsorbed **1a**$^{•+}$ is stabilized by electrostatic interaction with the $(Ag_3PO_4)^{n-}$ surfaces. The low possibility recombination between **1a**$^{•+}$ and e_{CB}^- shared by multiple Ag^+ cations, $(Ag^{\delta+})_m^-$, is evidenced by the observation of AgNP formation. As a result, the lifetime of **1a**$^{•+}$ is dramatically prolonged to > 2 ms, which is over 75 times longer than in a homogeneous solution (μs level[54]). The long lifetime of **1a**$^{•+}$ benefits the nucleophilic attack by another adsorbed **1a** molecule, allowing the reaction of **1a** + **1a**$^{•+}$ → **2a**$^{•+}$ in step IV to proceed (the RLS; see Supplementary Information for analysis).

The final step (step V) is the ring closure reaction of **2a**$^{•+}$. The potential of **2a**$^{•+}$/**2a** is approximately +1.5 V vs. NHE, much higher than the E_{CB} of Ag_3PO_4. Thermodynamically, the transfer of an electron from the reduced Ag_3PO_4 to **2a**$^{•+}$ is an exothermic reaction. Step V may also occur through a radical chain mechanism[22]. Considering the potential of **1a**$^{•+}$/**1a**, which is approximately +1.3 V vs. NHE, the ring closure of **2a**$^{•+}$ by e_{CB}^- exhibits a much larger driving force than that by the radical chain process.

The ability to generate the long-lived radical cation **1a**$^{•+}$ distinguishes $(Ag_3PO_4)^{n-}$ from a traditional photocatalytically reduced TiO_2 NP. On the illuminated TiO_2 NP, the lifetime of **1a**$^{•+}$ was too short to detect, and the conversion was only 18% (Fig. 3d). Okada et al. used a substantial excess of TiO_2 (e.g., > 6 equiv) to minimize the accumulated electron per NP and extra $LiClO_4$ (1.0 M) to stabilize the radical cations[18,22,23,25–27]. In contrast, Ag_3PO_4 photocatalysis can harvest the visible spectrum of sunlight and achieve a high yield of the desired product without any additives.

Discussion

Ag_3PO_4 is a powerful photocatalyst for homo, crossed, intramolecular [2 + 2], and Diels-Alder [4 + 2] pericyclic reactions under visible-light irradiation. The catalytic process is mild, straightforward, affordable, additive-free, scalable under sunlight irradiation, and allows for easy product separation and catalyst reuse. It has a broad substrate scope and produces a wide range of desired products in modest to excellent yields. Our study reveals the potential of this photocatalytic process
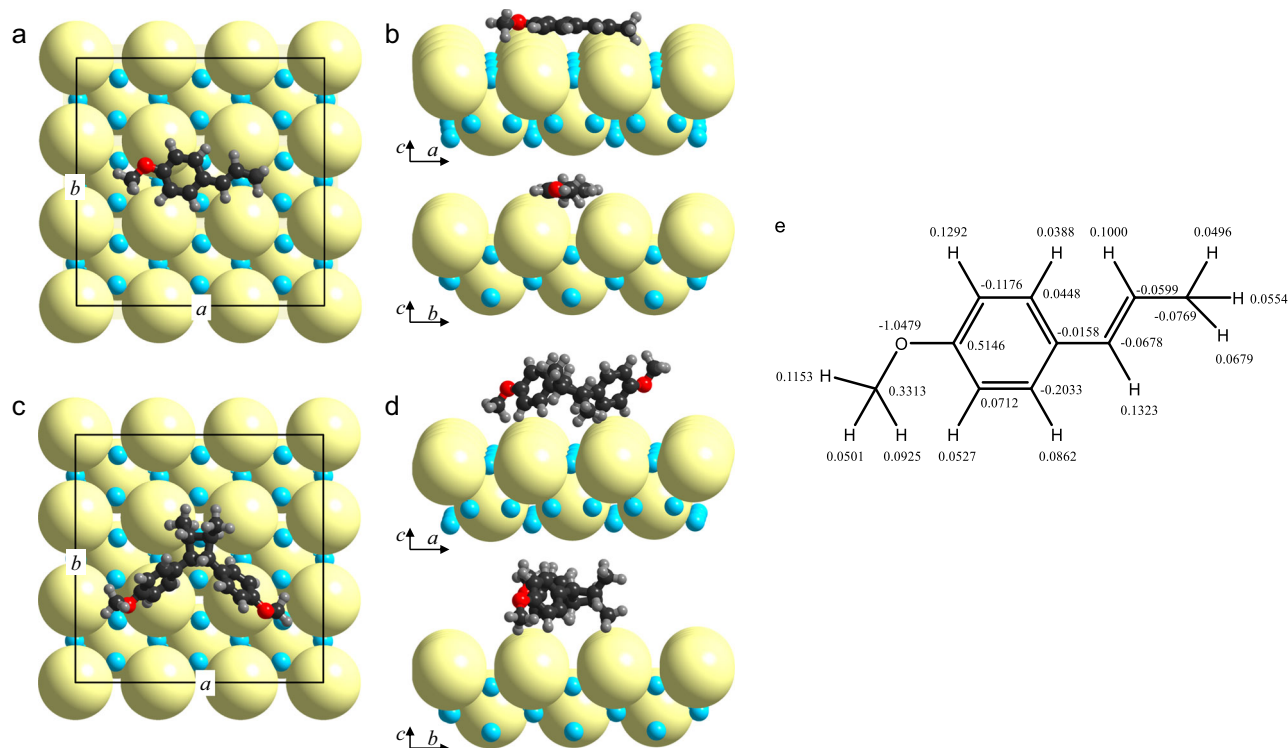
Fig. 8 | Configurations of adsorption and Bader charge. a–d The lowest-energy configurations of **1a** and **2a** molecules on the 2 × 2 region of the PO_4^{3-}-terminated (100) facet of Ag_3PO_4. **a** and **c** are the top views. **b** and **d** are the side views. The labels *a* and *b* denote the cell axes. The pale-yellow spheres represent PO_4^{3-} (*r* = 2.38 Å), and the cyan spheres represent Ag^+ (*r* = 0.67 Å). **1a** and **2a** molecules are drawn to scale. **e** The atomic Bader charges of adsorbed **1a**.
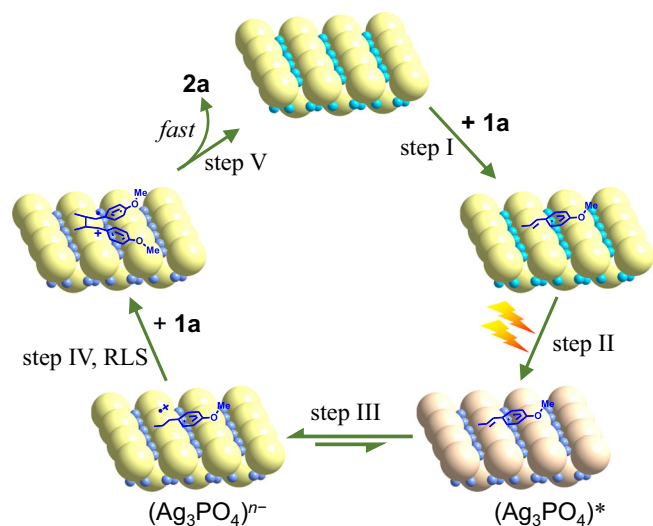

Fig. 9 | A plausible mechanism. $(Ag_3PO_4)^*$ denotes a photo-excited Ag_3PO_4 NP with many e_{CB}^- and h^+. The purple-blue spheres are used to show that in $(Ag_3PO_4)^*$ and $(Ag_3PO_4)^{n-}$, the e_{CB}^- is shared by silver cations, resulting in a fraction charge of $\delta+$ ($0 < \delta < 1$) on each cation.

for fine chemical production. We have demonstrated that the rate-limiting step is the reaction between the reactant and its 1e-oxidation intermediate, a radical cation. The lifetime of anethole radical cation (**1a**$^{•+}$) on the Ag_3PO_4 surfaces exceeds 2 ms, which is over 75 times longer than that in the homogeneous solutions, thus effectively promoting the rate-limiting step. The long lifetime of **1a**$^{•+}$ is attributed to the appropriate band structure of Ag_3PO_4 and the strong electrostatic interaction between **1a**$^{•+}$ and the $(Ag_3PO_4)^{n-}$ NP surfaces, which should

be a general and essential mechanism for promoting chemical processes mediated by radical cations on heterogeneous surfaces. This may inspire ideas for more challenging radical cation/anion-mediated solar synthesis using inorganic semiconductor photocatalysts.

Methods

General procedure for the photocatalytic reactions
The reactions were carried out in 10-mL Pyrex vials. Olefin and Ag_3PO_4 were dispersed in a solvent in the vial, which was then purged for 10 min with high-purity N_2 (99.999%). The vial was immersed in a mixture of ice and water to maintain the reaction temperature. The reaction suspension was stirred in the dark for 30 min to achieve adsorption-desorption equilibrium. The mixture was then exposed to the lamp from the side. To monitor the reaction progress, a syringe was used to withdraw 10 µL of the solution for analysis by thin-layer chromatography (TLC). After the reaction, the suspension was centrifuged to separate the solid catalyst from the solution. The residue is purified with column chromatography to afford the desired pure products.

Details for the homo-dimerization of aromatic alkenes
To a solution of aromatic alkene **1** (1.0 mmol) in 3.0 mL of HFIP, Ag_3PO_4 (27 mg, 0.12 equiv) was added in one portion. The remaining steps are the same as the general procedure.

Details for the cross-dimerization of aromatic alkenes
To a solution of aromatic alkene **3** (1.0 mmol, 2.0 equiv) in 2.0 mL of HFIP was added Ag_3PO_4 (44 mg, 0.20 equiv). Then, the reaction mixture was degassed by purging with high-purity nitrogen for 10 min. An ice bath was used to maintain the reaction temperature. The mixture was stirred in the dark at 0 °C for half an hour to achieve adsorption-desorption equilibrium. The photocatalytic reaction was then initiated by irradiating the dispersion from the side with the LED lamps. During

the reaction, a solution of **1** (0.5 mmol) in 2.0 mL HFIP was added using a syringe pump (at a rate of 4.0 mL/h). The remaining steps are the same as the general procedure.

Details for the intramolecular [2 + 2] reactions
To a solution of aromatic alkene **5** (0.3 mmol) in 2.0 mL of HFIP, Ag$_3$PO$_4$ (12 mg, 0.10 equiv) was added in one portion. The remaining steps are the same as the general procedure.

Details for the Diels–Alder cycloadditions
To a solution of the diene **7** (2.0 mmol, 2.0 equiv) in 2.0 mL of HFIP was added Ag$_3$PO$_4$ (32 mg, 0.08 equiv). Then, the reaction mixture was degassed by purging with high-purity nitrogen for 10 min. An ice bath was used to maintain the reaction temperature. The mixture was then stirred in the dark at 0 °C for half an hour to achieve adsorption-desorption equilibrium. The photocatalytic reaction was initiated by irradiating the dispersion from the side with an LED lamp. During the reaction, a solution of **1** (1.0 mmol) in 2.0 mL of HFIP was added using a syringe pump (at a rate of 4.0 mL/h). The remaining steps are the same as the general procedure.

Data availability
The authors declare that all relevant data supporting the findings of this study are available either within the manuscript itself and/or in the Supplementary Information. Experimental details and characterization of products are provided in the Supplementary Information. All other data are available from the corresponding author upon request. Source data are provided in this paper.

References
1. Nair, V., Rajan, R., Mohanan, K. & Sheeba, V. Cerium(iv) ammonium nitrate-mediated oxidative rearrangement of cyclobutanes and oxetanes. *Tetrahedron Lett.* **44**, 4585–4588 (2003).
2. Yu, Y., Fu, Y. & Zhong, F. Benign catalysis with iron: facile assembly of cyclobutanes and cyclohexenes via intermolecular radical cation cycloadditions. *Green Chem.* **20**, 1743–1747 (2018).
3. Colomer, I., Coura Barcelos, R. & Donohoe, T. J. Catalytic hypervalent iodine promoters lead to styrene dimerization and the formation of tri- and tetrasubstituted cyclobutanes. *Angew. Chem. Int. Ed.* **55**, 4748–4752 (2016).
4. Colomer, I., Batchelor-McAuley, C., Odell, B., Donohoe, T. J. & Compton, R. G. Hydrogen bonding to hexafluoroisopropanol controls the oxidative strength of hypervalent iodine reagents. *J. Am. Chem. Soc.* **138**, 8855–8861 (2016).
5. Liu, X. et al. Unraveling the structure and reactivity patterns of the indole radical cation in regioselective electrochemical oxidative annulations. *J. Am. Chem. Soc.* **145**, 3175–3186 (2023).
6. Ischay, M. A., Lu, Z. & Yoon, T. P. [2+2] cycloadditions by oxidative visible light photocatalysis. *J. Am. Chem. Soc.* **132**, 8572–8574 (2010).
7. Yoon, T. P., Ischay, M. A. & Du, J. Visible light photocatalysis as a greener approach to photochemical synthesis. *Nat. Chem.* **2**, 527–532 (2010).
8. Jiang, M., Yang, H. & Fu, H. Visible-light photoredox borylation of aryl halides and subsequent aerobic oxidative hydroxylation. *Org. Lett.* **18**, 5248–5251 (2016).
9. Tian, Y. M. et al. Visible-light-induced Ni-catalyzed radical borylation of chloroarenes. *J. Am. Chem. Soc.* **142**, 18231–18242 (2020).
10. Tian, Y. M. et al. Selective photocatalytic C-F borylation of polyfluoroarenes by Rh/Ni dual catalysis providing valuable fluorinated arylboronate esters. *J. Am. Chem. Soc.* **140**, 17612–17623 (2018).
11. Zhang, L., Si, X., Rominger, F. & Hashmi, A. S. K. Visible-light-induced radical carbo-cyclization/gem-diborylation through triplet energy transfer between a gold catalyst and aryl iodides. *J. Am. Chem. Soc.* **142**, 10485–10493 (2020).
12. Mazzarella, D., Magagnano, G., Schweitzer-Chaput, B. & Melchiorre, P. Photochemical organocatalytic borylation of alkyl chlorides, bromides, and sulfonates. *ACS Catal.* **9**, 5876–5880 (2019).
13. Zhang, L. & Jiao, L. Visible-light-induced organocatalytic borylation of aryl chlorides. *J. Am. Chem. Soc.* **141**, 9124–9128 (2019).
14. Chen, J., Cen, J., Xu, X. & Li, X. The application of heterogeneous visible light photocatalysts in organic synthesis. *Catal. Sci. Technol.* **6**, 349–362 (2016).
15. Jin, S. et al. Visible light-induced borylation of C-O, C-N, and C-X bonds. *J. Am. Chem. Soc.* **142**, 1603–1613 (2020).
16. Al-Ekabi, H. & De Mayo, P. Surface photochemistry: the CdS photoinduced dimerization of n-vinylcarbazole. *Tetrahedron* **42**, 6277–6284 (1986).
17. Liu, Y., Zhang, M., Tung, C.-H. & Wang, Y. TiO$_2$ photocatalytic cyclization reactions for the syntheses of aryltetralones. *ACS Catal.* **6**, 8389–8394 (2016).
18. Farney, E. P. et al. Discovery and elucidation of counteranion dependence in photoredox catalysis. *J. Am. Chem. Soc.* **141**, 6385–6391 (2019).
19. Horibe, T., Ohmura, S. & Ishihara, K. Structure and reactivity of aromatic radical cations generated by FeCl$_3$. *J. Am. Chem. Soc.* **141**, 1877–1881 (2019).
20. Okada, Y. Redox-neutral radical-cation reactions: Multiple carbon–carbon bond formations enabled by single-electron transfer. *Electrochemistry* **88**, 497–506 (2020).
21. Horiguchi, G., Kamiya, H. & Okada, Y. Mechanistic studies on TiO$_2$ photoelectrochemical radical cation [2 + 2] cycloadditions. *J. Electrochem. Soc.* **167**, 155529 (2020).
22. Das, S. et al. Asymmetric counteranion-directed photoredox catalysis. *Science* **379**, 494–499 (2023).
23. Horibe, T., Katagiri, K. & Ishihara, K. Radical-cation-induced crossed [2+2] cycloaddition of electron-deficient anetholes initiated by iron(iii) salt. *Adv. Synth. Catal.* **362**, 960–963 (2020).
24. Wang, Y., Wei, Y., Song, W., Chen, C. & Zhao, J. Photocatalytic hydrodehalogenation for the removal of halogenated aromatic contaminants. *ChemCatChem* **11**, 258–268 (2019).
25. Ghosh, I. et al. Organic semiconductor photocatalyst can bifunctionalize arenes and heteroarenes. *Science* **365**, 360–366 (2019).
26. Nakayama, K., Kamiya, H. & Okada, Y. Radical cation Diels-Alder reactions of arylidene cycloalkanes. *Beilstein J. Org. Chem.* **18**, 1100–1106 (2022).
27. Adachi, S., Horiguchi, G., Kamiya, H. & Okada, Y. Photochemical radical cation cycloadditions of aryl vinyl ethers. *Eur. J. Org. Chem.* **2022**, e202201207 (2022).
28. Okada, Y. "Snapshots" of intramolecular electron transfer in redox tag-guided [2 + 2] cycloadditions. *J. Org. Chem.* **84**, 1882–1886 (2019).
29. Okada, Y., Maeta, N., Nakayama, K. & Kamiya, H. TiO$_2$ photocatalysis in aromatic "redox tag"-guided intermolecular formal [2 + 2] cycloadditions. *J. Org. Chem.* **83**, 4948–4962 (2018).
30. Horiguchi, G. & Okada, Y. Mechanistic understanding of electrocatalytic vinylcyclopropane rearrangement. *Eur. J. Org. Chem.* **2022**, e202201022 (2022).
31. Maeta, N., Kamiya, H. & Okada, Y. Probing intramolecular electron transfer in redox tag processes. *Org. Lett.* **21**, 8519–8522 (2019).
32. Nakayama, K., Maeta, N., Horiguchi, G., Kamiya, H. & Okada, Y. Radical cation Diels–Alder reactions by TiO$_2$ photocatalysis. *Org. Lett.* **21**, 2246–2250 (2019).
33. Maeta, N., Kamiya, H. & Okada, Y. Radical-cation vinylcyclopropane rearrangements by TiO$_2$ photocatalysis. *J. Org. Chem.* **85**, 6551–6566 (2020).

34. Linsebigler, A. L., Lu, G. & Yates, J. T. Photocatalysis on TiO$_2$ surfaces: Principles, mechanisms, and selected results. *Chem. Rev.* **95**, 735–758 (1995).

35. Yi, Z. et al. An orthophosphate semiconductor with photooxidation properties under visible-light irradiation. *Nat. Mater.* **9**, 559–564 (2010).

36. Martin, D. J., Umezawa, N., Chen, X., Ye, J. & Tang, J. Facet engineered Ag$_3$PO$_4$ for efficient water photooxidation. *Energy Environ. Sci.* **6**, 3380–3386 (2013).

37. Bi, Y., Ouyang, S., Umezawa, N., Cao, J. & Ye, J. Facet effect of single-crystalline Ag$_3$PO$_4$ sub-microcrystals on photocatalytic properties. *J. Am. Chem. Soc.* **133**, 6490–6492 (2011).

38. Martin, D. J. et al. Efficient visible driven photocatalyst, silver phosphate: performance, understanding and perspective. *Chem. Soc. Rev.* **44**, 7808–7828 (2015).

39. Ischay, M. A., Ament, M. S. & Yoon, T. P. Crossed intermolecular [2 + 2] cycloaddition of styrenes by visible light photocatalysis. *Chem. Sci.* **3**, 2807–2811 (2012).

40. Riener, M. & Nicewicz, D. A. Synthesis of cyclobutane lignans via an organic single electron oxidant-electron relay system. *Chem. Sci.* **4**, 2625–2629 (2013).

41. Guo, L., Cui, E., Li, H., Tung, C.-H. & Wang, Y. Singlet oxygen- and hole-mediated selective oxidation of arylethylenes to aryltetralones by Ag/Ag$_3$PO$_4$ under visible light irradiation. *ACS Sustainable Chem. Eng.* **9**, 16670–16677 (2021).

42. Cui, E. et al. Engaging Ag(0) single atoms in silver(i) salts-mediated C-B and C-S coupling under visible light irradiation. *J. Catal.* **402**, 255–263 (2021).

43. An, C. et al. Plasmonic silver incorporated silver halides for efficient photocatalysis. *J. Mater. Chem. A* **4**, 4336–4352 (2016).

44. Cortie, M. B. & McDonagh, A. M. Synthesis and optical properties of hybrid and alloy plasmonic nanoparticles. *Chem. Rev.* **111**, 3713–3735 (2011).

45. An, C., Peng, S. & Sun, Y. Facile synthesis of sunlight-driven AgCl:Ag plasmonic nanophotocatalyst. *Adv. Mater.* **22**, 2570–2574 (2010).

46. Garg, R., Mondal, S., Sahoo, L., Vinod, C. P. & Gautam, U. K. Nanocrystalline Ag$_3$PO$_4$ for sunlight- and ambient air-driven oxidation of amines: high photocatalytic efficiency and a facile catalyst regeneration strategy. *ACS Appl. Mater. Interfaces* **12**, 29324–29334 (2020).

47. Yang, C. et al. Heterogeneous photoredox flow chemistry for the scalable organosynthesis of fine chemicals. *Nat. Commun.* **11**, 1239 (2020).

48. Jiang, Y., Wang, C., Rogers, C. R., Kodaimati, M. S. & Weiss, E. A. Regio- and diastereoselective intermolecular [2+2] cycloadditions photocatalysed by quantum dots. *Nat. Chem.* **11**, 1034–1040 (2019).

49. Zhao, Y. & Antonietti, M. Visible-light-irradiated graphitic carbon nitride photocatalyzed Diels–Alder reactions with dioxygen as sustainable mediator for photoinduced electrons. *Angew. Chem. Int. Ed.* **56**, 9336–9340 (2017).

50. Lin, S., Ischay, M. A., Fry, C. G. & Yoon, T. P. Radical cation Diels-Alder cycloadditions by visible light photocatalysis. *J. Am. Chem. Soc.* **133**, 19350–19353 (2011).

51. Pitre, S. P., Scaiano, J. C. & Yoon, T. P. Photocatalytic indole Diels-Alder cycloadditions mediated by heterogeneous platinum-modified titanium dioxide. *ACS Catal.* **7**, 6440–6444 (2017).

52. Pitre, S. P., Yoon, T. P. & Scaiano, J. C. Titanium dioxide visible light photocatalysis: Surface association enables photocatalysis with visible light irradiation. *Chem. Commun.* **53**, 4335–4338 (2017).

53. Johnston, L. J. & Schepp, N. P. Reactivities of radical cations: characterization of styrene radical cations and measurements of their reactivity toward nucleophiles. *J. Am. Chem. Soc.* **115**, 6564–6571 (1993).

54. Schepp, N. P. & Johnston, L. J. Reactivity of radical cations. Absolute kinetic data for cycloaddition reactions of styrene radical cations to alkenes. *J. Am. Chem. Soc.* **116**, 10330–10331 (1994).

55. Cismesia, M. A. & Yoon, T. P. Characterizing chain processes in visible light photoredox catalysis. *Chem. Sci.* **6**, 5426–5434 (2015).

56. Cozens, F. L. et al. Photochemical and thermal behavior of styrenes within acidic and nonacidic zeolites. Radical cation versus carbocation formation. *J. Phys. Chem. B* **101**, 6921–6928 (1997).

57. Hsieh, M. S., Su, H. J., Hsieh, P. L., Chiang, Y. W. & Huang, M. H. Synthesis of Ag$_3$PO$_4$ crystals with tunable shapes for facet-dependent optical property, photocatalytic activity, and electrical conductivity examinations. *ACS Appl. Mater. Interfaces* **9**, 39086–39093 (2017).

58. Ke, J. et al. Facet-dependent electrooxidation of propylene into propylene oxide over Ag$_3$PO$_4$ crystals. *Nat. Commun.* **13**, 932 (2022).

59. Xiong, Y. et al. Single-atom Rh/N-doped carbon electrocatalyst for formic acid oxidation. *Nat. Nanotechnol.* **15**, 390–397 (2020).

60. Hou, Y. et al. Ag$_3$PO$_4$ oxygen evolution photocatalyst employing synergistic action of Ag/AgBr nanoparticles and graphene sheets. *J. Phys. Chem. C* **116**, 20132–20139 (2012).

61. Bi, Y., Ouyang, S., Cao, J. & Ye, J. Facile synthesis of rhombic dodecahedral AgX/Ag$_3$PO$_4$ (X = Cl, Br, I) heterocrystals with enhanced photocatalytic properties and stabilities. *Phys. Chem. Chem. Phys.* **13**, 10071–10075 (2011).

Acknowledgements

Author contributions

Y.W. and C.T. conceived the idea and directed the project. L.G. performed the experiments and analyzed the data. R.C., X.H., Y.L., and H.L.; D.M. participated in characterization studies. G.W. performed the DFT calculation. Y.W. and L.G. wrote the manuscript, and L.G. prepared the Supplementary Information.

Competing interests

The authors declare no competing interests.

Additional information

Supplementary information The online version contains supplementary material available at
https://doi.org/10.1038/s41467-024-45217-y.

Correspondence and requests for materials should be addressed to Yifeng Wang.

Peer review information *Nature Communications* thanks Takashi Koike and the other, anonymous, reviewer(s) for their contribution to the peer review of this work. A peer review file is available.

Reprints and permissions information is available at
http://www.nature.com/reprints

Publisher's note Springer Nature remains neutral with regard to jurisdictional claims in published maps and institutional affiliations.